

Control of Crossflow-Vortex Induced Transition: DNS of Pinpoint Suction

Tillmann A. Friederich* and Markus J. Kloker†

Institut für Aerodynamik und Gasdynamik, Universität Stuttgart, D-70550 Stuttgart, Germany

Laminar-turbulent breakdown in a swept-wing boundary layer is typically caused by secondary instabilities of steady crossflow vortices (CFVs). So far, boundary-layer suction for laminar flow control in three-dimensional boundary layers has been applied to reduce the crossflow and thus the growth of the primary vortices only. We investigate the influence of strong, localized suction (*pinpoint suction*) on high-amplitude CFVs and their secondary instability. The highly concentrated suction necessary enforces however a high wall-normal resolution near the wall and careful grid studies to get converged results with our incompressible code based on the vorticity-velocity formulation of the equations. We show the successful application of *pinpoint suction* resulting in a significant delay of laminar-turbulent transition. The incompressible results are verified with our compressible code at $Ma=0.2$ using modeled suction holes. For $Ma=0.8$ we compare a modeled-suction result with a simulation that includes the interaction of the boundary-layer flow with the suction-channel flow.

Nomenclature

Subscript

∞	reference value
0	fundamental value
0.8	case at $Ma=0.8$
b	base flow value
c	compressible
e	edge value: at the upper boundary
i	incompressible
r	arbitrarily rotated coordinate
s	streamwise coordinate
<i>mod</i>	modeled
<i>chan</i>	channel

Superscript

'	disturbance value
-	dimensional value

Greek letters

α_i	amplification rate
β	timewise wave number
γ	spanwise wave number
δ_1	displacement thickness
λ_z	spanwise wave length
ϕ	local flow angle

$\bar{\nu}_\infty$	reference kinematic viscosity, m^2/s
$\bar{\rho}_\infty$	reference density, m^3/s

Latin letters

H_{12}	shape parameter
\bar{L}	reference length, m
\bar{p}_∞	reference pressure, N/m^2
\bar{T}_∞	reference temperature, K
\bar{U}_∞	reference velocity m/s
Re	Reynolds number
Ma	Mach number
CFV	cross flow vortex
KMAX	number of spanwise Fourier modes
d	suction hole diameter channel diameter
h	timewise harmonic
k	spanwise harmonic
\dot{m}	mass flow
t	time
(x, y, z)	chordwise, wall-normal, spanwise coordinates
(u, v, w)	corresponding velocity components
(r, h, ϕ)	cylindrical coordinates
(ξ, η, ζ)	rotated coordinates

*Research Assistant, AIAA Member

†Associate Professor, AIAA Member

I. Introduction

During the last decades both ecological and economical reasons led to a strong demand on laminar-flow-control technology development. Little potential is thought to be left in research areas like enhanced shaping and higher surface quality of wetted areas or engine improvement, but the overall drag of a current airliner with nearly fully turbulent flow could be reduced by 16% if the flow over 40% of the aerodynamic surfaces were laminar¹⁴. Nowadays, the two-dimensional breakdown caused by Tollmien-Schlichting (T-S) waves can be successfully controlled, see e.g. references^{9,12} (albeit not yet applied at airliner cruise conditions). In a three-dimensional boundary layer however the physical mechanism of transition to turbulence is completely different and methods like T-S wave cancelation cannot be applied.

Detailed studies on the three-dimensional transition process have been carried out in the last decades: Experiments¹⁸, theoretical results⁸ and direct numerical simulation (DNS)^{16,17} entirely revealed the secondary instability mechanism of CFVs. Several control methods have been developed since: Saric et al.¹³ proposed the distributed roughness elements method (DRE), where a one-time excitation of closely spaced steady CFVs generates a (secondarily) more stable flow scenario and thus delays transition. The concept of upstream flow deformation (UFD), suggested by Wassermann & Kloker^{15,16}, pursues the same goal, not necessarily connected to roughness. Messing & Kloker^{7,11} proposed a combination of UFD and suction, called distributed flow deformation (DFD) or formative suction, that aims at a persistent suppression of (secondarily) unstable CFVs in altering base flows.

Investigations by Bonfigli & Kloker³ revealed that the amplification of secondary instability modes of CFVs depends rather strongly on the wall-normal velocity component of the underlying base flow which lead to the initial idea of pinpoint suction by Friederich & Kloker⁴. In the current paper we show three major findings elaborated since the first application of pinpoint suction shown in our papers^{4,7}. First, as it turned out, our incompressible numerical method *N3D* needs an extremely fine wall-normal grid at the wall when strong suction is applied to obtain converged results. This is due to the vorticity formulation and the strong velocity gradients at the wall invoked by strong suction. Second, we compare results for a reference case and one selected *pinpoint-suction* case with results from our compressible code *NS3D* at Ma=0.2 to verify our incompressible results. To show the practical relevance of all these cases employing modeled suction at the wall, we finally compare a compressible case at Ma=0.8 with a simulation that includes the interaction with the suction channel.

Our paper is organized as follows: §II introduces the numerical methods and base flows and §III explains the pinpoint suction concept. §IV provides results for various incompressible pinpoint suction cases, for the compressible cases with modeled suction holes and included suction channel, respectively.

II. Numerical Methods

For both numerical methods all flow variables are non-dimensionalized with reference values including the reference length \bar{L} , chordwise velocity \bar{U}_∞ , Reynolds number $Re = \bar{U}_\infty \bar{L} / \bar{\nu}_\infty$, and in addition for the compressible case \bar{T}_∞ and $\bar{\rho}_\infty$, where the bar denotes dimensional values.

II.A. Incompressible Code *N3D*

N3D solves the incompressible three-dimensional Navier-Stokes equations in velocity-vorticity formulation. All flow quantities are split into a steady part (base flow) and an unsteady part, $q = q_B + q'$, to ease the formulation of boundary conditions. The time mean $\langle q' \rangle$ is non-zero for large q' . Sixth-order compact finite differences are used to discretize the streamwise (x) and wall-normal (y) directions. A Fourier spectral ansatz with $KMAX + 1$ modes is chosen for the spanwise direction z , where the fundamental wavelength is defined as $\lambda_{z,0} = 2\pi/\gamma_0$. The integration domain is shown in Fig. 1, and for the detailed method see references^{3,16}.

Instead of using our explicit standard fourth-order Runge-Kutta time-integration scheme a semi-implicit method has been developed due to the prohibitive viscous time-step limit caused by the necessary fine y -resolution at the wall. A three-stage second-order predictor-corrector method has been set up that is based on Heun's method with an additional corrector step to secure A-stability for the explicitly treated convective terms. In this method the viscous terms in wall-normal direction are simultaneously treated by the fully implicit trapezoidal rule. In addition, an iteration method is necessary for the vorticity equations at the wall (see Eq. 2.15 in reference¹⁶). The convective terms in y -direction still impose a small time

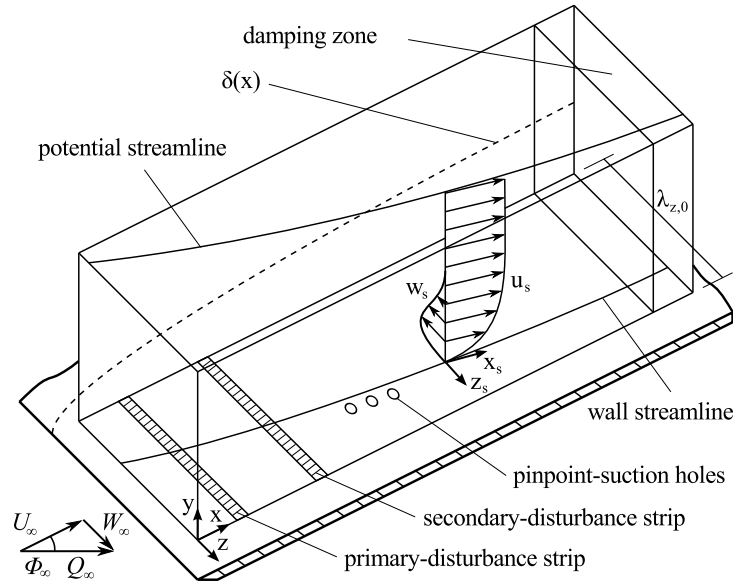


Figure 1. Integration domain, body-fixed (x, y, z) and streamline-oriented (x_s, y, z_s) coordinate systems.

step that required the implementation of a spatial filter in x -direction since the slightly dissipative forward-backward differencing for the convective terms in x -direction did not provide enough damping of numerical high wavenumber modes due to the small time step.

II.B. Compressible Code *NS3D*

NS3D solves the compressible three-dimensional Navier-Stokes equations in conservative formulation and total variables, where $\vec{Q} = (\rho, \rho u, \rho v, \rho w, E)^T$ represents the solution vector. The specific heat capacities c_p and c_v as well as the Prandtl number are assumed to be constant whereas temperature-viscosity dependence is modeled by Sutherland's law. Similarly to the incompressible code a rectangular integration domain on a flat plate is considered with similar nomenclature and discretization. In contrast to *N3D*, *NS3D* computes mainly in physical space and the Fourier space is used for obtaining the z -derivatives only. For time integration a standard explicit fourth-order Runge-Kutta method is used. For numerical details see references^{1,10}. For simulations including the suction channel a cylindrical coordinate system is used for the channel domain spanned by radius, wall-normal and azimuthal coordinate (r, h, ϕ) .

II.C. Implementation of Suction

For both codes the suction holes are modeled similarly within the wall boundary condition. The wall-parallel velocity components (u, w) are set to zero, and the wall-normal velocity component $v|_{wall}$ (*N3D*) or the wall-normal mass flux $\rho v|_{wall}$ (*NS3D*) are prescribed by a $\cos^3(r)$ -function where r is the hole radius. The maximum velocity in the hole center is $|v|_{max}/U_\infty = 0.5$. For the compressible case, this is checked in a post-processing step ($\rho v \Rightarrow v$). Details on the suction implementation can be found in reference¹¹.

The cases with suction channel employ boundary conditions at the lower suction channel outlet where values for the three velocity components u, v, w as well as the temperature T are extrapolated from the flow field. The pressure is set explicitly, and ρ results from the perfect gas equation. The pressure is adapted such that a specified mass flow is accomplished.

II.D. Base Flows and Simulation Setups

The base flow is taken from the DLR-Prinzipexperiment Göttingen², see also Bonfigli & Kloker³. The free-stream velocity \bar{U}_∞ is 14 m/s in the experiment, with chordwise Mach number $Ma_\infty \approx 0.04$. For the low-Mach-number case $Ma=0.2$ has been chosen ensuring predominantly incompressible behavior at a non-prohibitive time step. (Note that $\Delta t \sim Ma_\infty^q$, where $q \approx 1$ for dominating convective terms, and $q \approx 2$ for dominating viscous terms. At $Ma=0.2$ both are of same order related to the y -direction and hence $\Delta t \sim Ma_\infty^2$ for $Ma_\infty < 0.2$.) The integration domains cover the same Re_{δ_1} range to ensure flow similarity.

	<i>incompressible setup</i> cases with subscript <i>i</i>	<i>compressible setup</i> subscript <i>c</i> , $Ma=0.2$ $Ma=0.8$
x_0	1.655	1.900
$\Delta x \times 10^3$	1.309	1.309
$\Delta y_{wall} \times 10^4$	0.066	2.300
$\Delta y_e / \Delta y_{wall}$	120	12
y_e	0.077	0.116 0.078
$\Delta z \times 10^3$	1.873	3.747
KMAX	15 (10)	10
γ_0	52.400	52.400
$\Delta t \times 10^5$	6.550	1.047
grid points $x \times y \times z$	$3202 \times 225 \times 32$	$1816 \times 95 \times 32$
channel grid $r \times h \times \phi$	-	- $14 \times 1000 \times 32$
$Re = \bar{U}_\infty \bar{L} / \bar{\nu}_\infty$	92000	92000
$Ma_\infty = \bar{U}_\infty / \bar{a}_\infty$	-	0.21 0.84
\bar{L}	0.10 m	$1.92 \cdot 10^{-2}$ m $4.81 \cdot 10^{-3}$ m
$\bar{\nu}_\infty$	$1.52 \cdot 10^{-5}$ m ² /s	$1.52 \cdot 10^{-5}$ m ² /s
\bar{U}_∞	14.00 m/s	72.72 m/s 290.87 m/s
$\bar{W}_\infty = \bar{W}_e$	12.83 m/s	66.63 m/s 266.54 m/s
$\bar{T}_\infty = \bar{T}_{wall}$	-	303.40 K
\bar{p}_∞	-	1.0669 bar
Φ_∞	42.5°	42.5°
suction hole diameter d_{mod}	0.0262	0.0262 0.0262
maximum suction rate $ (\rho)v _{max}$	$ -0.500 $	$ -0.500 $ $ -0.436 $
channel diameter d_{chan}	-	- 0.0168
for one-hole cases:		
suction hole center (x, z)	(3.3602, 0.0600)	(3.3602, 0.0600) (3.3602, 0.0482)

Table 1. Simulation parameters for incompressible base flow and compressible base flows.

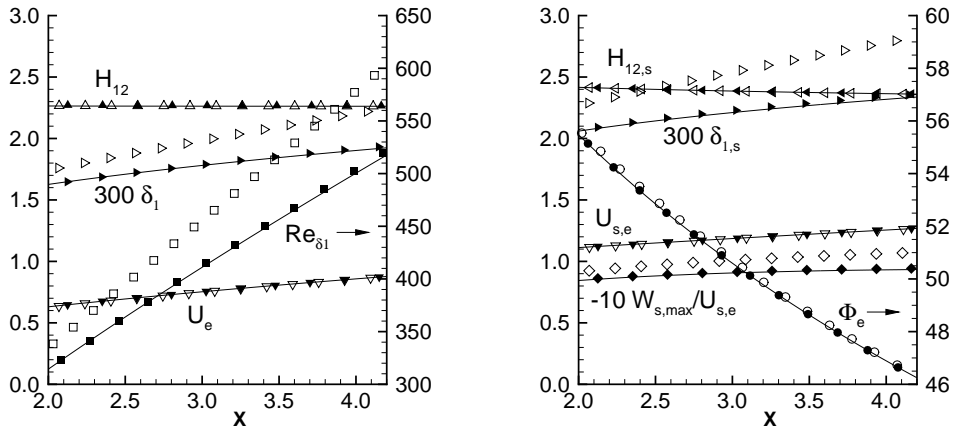


Figure 2. Boundary-layer parameters for incompressible base flow (lines) and compressible base flows (filled symbols for the $Ma=0.2$ case, empty symbols for the $Ma=0.8$ case). Right axes show Re_{δ_1} and Φ_e , respectively. Values in the right plot are based on $U_{s,e}$.

For the expensive simulation including the suction channel a third base flow is considered where the Mach number has been increased to $Ma_\infty \approx 0.8$ at identical Reynolds number. This corresponds to a four times smaller length scale while the velocity is four times higher compared to the $Ma=0.2$ case.

The compressible base flows are computed with *NS3D* using a solution of the parabolized Navier-Stokes equations as initial condition where the free-stream velocity $U_e(x)$ is chosen as design variable and prescribed to be identical to the incompressible case. Note that the base flows are two-dimensional (infinite wing-span assumption), but include a spanwise velocity component W , where the edge velocity W_e is kept constant. For the $Ma=0.2$ case the temperature T_b and density ρ_b vary less than by 0.5% within our integration domain (not shown) ensuring incompressible behavior.

The simulation parameters are given in Table 1 and a comparison of the respective boundary-layer parameters is shown in Fig. 2. Values obtained from the stream-line oriented velocity component u_s are marked with the subscript s . For all three base flows we use an incompressible evaluation of the boundary-layer parameters, i.e. neglecting density variation in order to investigate the influence of the velocity profiles only. The design variable u_e (and also $u_{s,e}$) shows three identical distributions. No significant deviations can be found neither for the shape parameters H_{12} and $H_{12,s}$ (ratio of displacement to momentum thickness, less than 0.3%) nor the local flow angle Φ_e (less than 0.4%). The curves for the displacement thickness δ_1 and $\delta_{1,s}$ and also Re_{δ_1} differ only marginally comparing the incompressible and $Ma=0.2$ case. The higher values for the $Ma=0.8$ case can be explained by stronger wall-normal motion of the fluid (comparing v -velocity profiles, not shown). This is a compensating effect for decreasing density in streamwise direction.

III. Secondary Instability and Pinpoint Suction Concept

The steady unstable primary crossflow vortex mode (0,1) is triggered at $x = 2.2$ through a disturbance strip at the wall (we use the common double-spectral notation (h,k) with frequencies $\beta = h \cdot \beta_0$ and spanwise wave numbers $\gamma = k \cdot \gamma_0$) where the wall-normal velocity component is prescribed^{3,16}. After the crossflow vortex has developed to a finite amplitude level, a pulse-like disturbance containing frequencies between $\beta = \beta_0 = 6.0$ and $\beta = 300.0$ with $\Delta\beta = 6.0$ is periodically excited at $x = 3.0$ (modes $(h, \pm 1)$, $h=1-50$) to initiate controlled secondary instability. This case is the incompressible reference case REF_i and later on the compressible case REF_c is simulated analogously prescribing ρv in the disturbance strips.

After a quasi-periodic state is reached the flow field is Fourier-analyzed to find unstable secondary modes and trace their respective maxima in downstream direction. The amplitude development of selected steady and unsteady modes of the streamline-oriented disturbance velocity component $\tilde{u}_s = u_s/U_{b,s,e}$ is shown in Fig. 3 where $U_{b,s,e}$ denotes the local base flow velocity in streamwise direction at the boundary-layer edge. The maximum three-dimensional steady deformation ($\beta = 0 - (0,0)$), i.e. the maximum amplitude of the zero-frequency disturbance in the $y - z$ crossplane diminished by the local mean flow deformation, serves as measure for the vortex strength. At $x = 3.0$ its amplitude level reaches 20% and explosive secondary growth

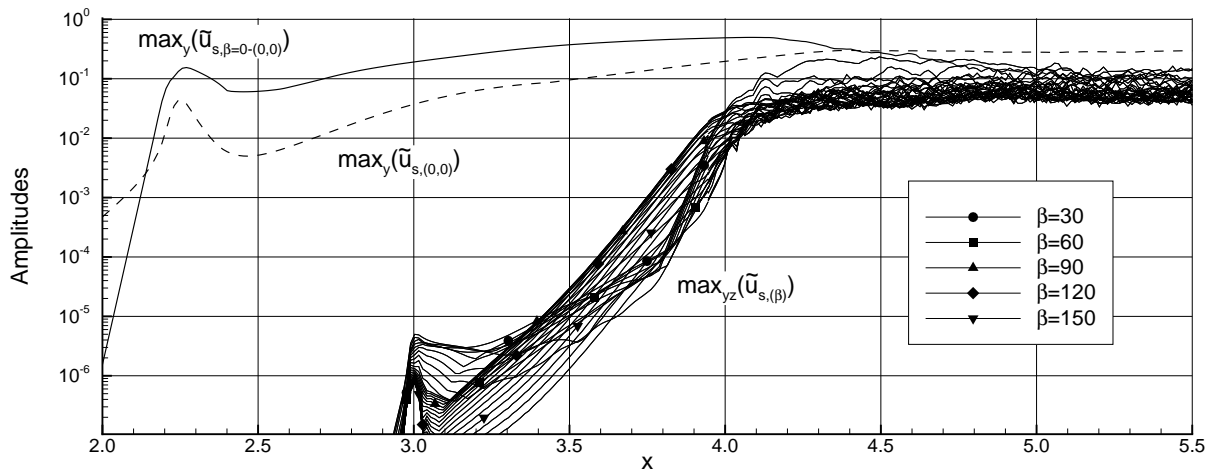


Figure 3. Downstream development of modal \tilde{u}'_s -amplitudes from Fourier analysis in time. Shown are the y -maxima of the mean flow deformation (0,0), the pure 3-D deformation $\beta = 0 - (0,0)$, and $y - z$ -maxima of unsteady modes for the incompressible reference case REF_i .

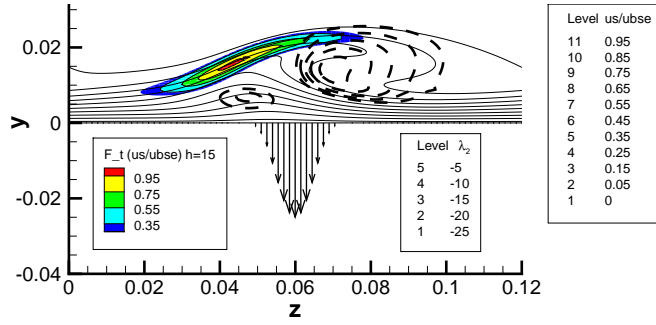


Figure 4. Pinpoint suction concept (case REF_i): Crosscut at $x = 3.36$ through a crossflow vortex without suction (lines: \bar{u}_s -isocontours; dashed lines: λ_2 -isocontours; colored: modal \bar{u}_s -amplitude distribution of high-frequency secondary instability mode $h=15$ ($\beta = 90$) and design example of pinpoint-suction position at the wall (arrows, crosscut through center of suction hole).

of high-frequency modes can be observed from the beginning of the pulse triggering. Starting at $x = 3.8$, non-linear growth of low-frequency modes can be detected and transition to turbulence begins soon after.

Fig. 4 shows the pinpoint suction setup. The crosscut reveals the main crossflow vortex (marked by the dashed λ_2 values), turning clockwise (looking in downstream direction), and the eigenfunction of the typical unstable secondary instability mode with $\beta = 90$ is concentrated at the location of the high-shear layer at the updraft side of the vortex. The suction hole position (marked by the arrows) is located right beneath this layer. Two effects are expected: On the one hand the growth of the main vortex is hindered since a counter-rotating movement of the fluid is actively forced, and on the other hand a wall-normal velocity component is imposed onto the shear-layer which can lead to a secondary-growth-rate reduction as discussed by Bonfigli & Kloker³.

IV. Results

IV.A. Incompressible DNS with modeled suction

The incompressible pinpoint suction scenarios are set up according to Fig. 4. Case 1-50 p_i is used as verification of the fundamental mechanism of *pinpoint suction* and later on (besides the reference case) as comparison for the compressible cases. One hole with $|v|_{max} = 0.5 U_\infty = 0.41 U_{s,e}$ is modeled at $x = 3.36$ with a diameter of $d = 0.0262$ which equals approximately the boundary-layer thickness and covers about 22% of one fundamental spanwise wavelength $\lambda_{z,0}$. To enhance the effect without increasing the maximum suction amplitude (and thus dodging wall-normal resolution problems) cases 3-50 p_i and 9-50 p_i are considered with three and nine (in vortex-core direction) succeeding holes, respectively. Case 3-50 p_i employs three identical holes at $x=3.36, 3.38, 3.40$, and for case 9-50 p_i the nine holes are equally spaced within $x \in [3.36, 3.52]$. In order to compare the three-dimensional contribution of pinpoint suction, a “two-dimensional” case is additionally simulated (case 3-2D $_i$) corresponding to case 3-50 p_i , i.e. only the spanwise average suction part is activated resulting in three consecutive 2-D slits with equivalent $c_q = \bar{v} \cdot P / \bar{U}_{s,e}$ (\bar{v} : average suction of the hole; P : porosity of the suction panel, $\bar{U}_{s,e}$: local streamwise edge velocity).

Fig. 5 shows the results for all cases. The pure steady 3-D deformation $\beta = 0 - (0, 0)$ shows different attenuation effects for the various suction scenarios. The evaluation of selected unsteady, high-frequency secondary instability modes reveals transition delay for all suction scenarios compared to the reference case REF_i . Case 1-50 p_i reveals considerable attenuation of secondary growth. The case with two-dimensional slit suction 3-2D $_i$ reveals similar results with respect to transition delay. Case 3-50 p_i , however, using the same suction amount as case 3-2D $_i$, achieves a significantly larger shift of the transition location. Note that also the steady 3-D part is reduced to a smaller amplitude level here. This verifies that the localization in a streamwise and spanwise sense and thus the three-dimensional contribution is an important parameter for pinpoint suction. Further investigations, not included in this paper, show that holes shifted in spanwise direction are less effective but do never expedite transition. For case 9-50 p_i secondary growth and thus transition is eliminated completely (see also reference⁶).

For the maximum suction velocity of $|v|_{max}/U_\infty = 0.5$ within the modeled approach, the incompressible simulations, based on the vorticity-velocity formulation, demand an extreme wall-normal resolution of

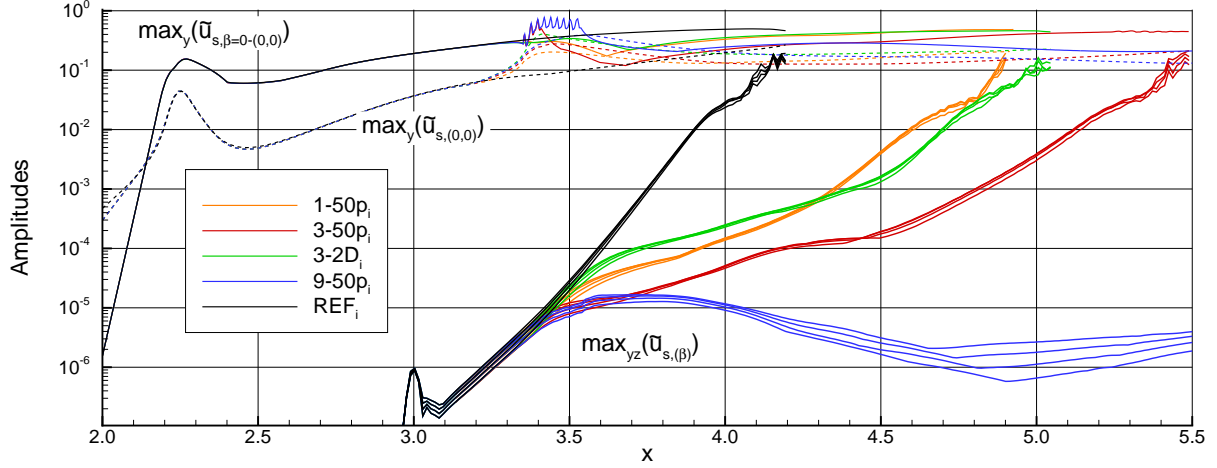


Figure 5. Downstream development of modal \tilde{u}'_s -amplitudes. Shown are the y -maxima of the mean flow deformation $(0,0)$, the pure 3-D deformation $\beta = 0 - (0,0)$, and $y - z$ -maxima of some important high-frequency modes $h=16, 17, 18, 19$ for the incompressible reference case and various incompressible suction scenarios.

$\Delta y_{wall} \approx \frac{1}{1100} \delta_1$ for converged results. Since there are, to our knowledge, no publications on strong suction in three-dimensional boundary layers available our compressible numerical method *NS3D* is chosen as verification source since it solves a different set of equations.

IV.B. Verification of incompressible modeled-suction results with compressible DNS

The reference case and the pinpoint-suction case with one suction hole are simulated with our compressible numerical method and compared to the incompressible results, hence four cases are considered in this chapter: REF_i , REF_c , $1-50p_i$, and $1-50p_c$.

The compressible-code simulation is carried out triggering identical perturbations as in the incompressible case (primary mode, secondary modes, see §III) resulting in case REF_c . Simulation parameters are given in Table 1. The downstream \tilde{u}'_s -amplitude development of selected steady and unsteady modes is shown in Fig. 6. (Note that for comparison the incompressible simulations use $KMAX=10$ here as well.) Virtually identical results can be observed. The growth rates ($x \in [3.3, 3.8]$) and also the non-linear behavior of mode $\beta = 36$ for $x > 3.9$ match perfectly.

For the compressible code the modeled suction hole is set up by prescribing the mass flux (ρv) at the wall. Since the density varies slightly the v -distribution is checked in a post-processing step and $|(\rho v)|_{max} = 0.46$ is used to match the incompressible distribution. The influence of the suction on the vortex strength ($\beta = 0 - (0,0)$) is again virtually identical. Also, low- and high-frequency growth rates ($\beta = 36, 90, x \in [3.5, 4.1]$) match.

As for the computational effort we note that, although $\Delta y_{wall,i} \approx 1/35 \Delta y_{wall,c}$, $\Delta t_i \approx 6 \Delta t_c$, and the numerical effort turns out to be still ten times larger for the compressible method. Thus a case with small integration-domain extensions and resolution was chosen as verification case. For more details see reference⁵.

IV.C. Compressible DNS at $Ma=0.8$ including suction channel

Two aspects have been taken into account for choosing a higher Mach number: First, compressible effects for cruise conditions are now included, and second, the numerical effort is considerably smaller for the expensive channel simulation, since $\Delta t \sim Ma_\infty$. The boundary-layer parameters have already been introduced in Fig. 2. We find a thicker boundary layer, as expected for a higher Ma number, even with the slightly cooled, isothermal wall. The maximum amplification rate of steady crossflow modes is shifted towards lower spanwise wave numbers and also the magnitude slightly decreases. The incompressible maximum is at $\gamma = 46.9$ and $\alpha_i = -2.50$ (gained by incompressible LST) while the compressible maximum is found at $\gamma = 42.3$ and $\alpha_i = -2.45$ (compressible LST). Mode $(0,1)$ with $\gamma = 52.4$ is triggered to keep the spanwise integration-domain extent as in the $Ma=0.2$ case.

Three cases are considered: the reference case $REF_{c,0.8}$, the case with modeled suction $1-50p_{c,0.8}$, and the case with the included suction channel $1-50p_{c,chan}$. For the latter a low pressure level is prescribed at

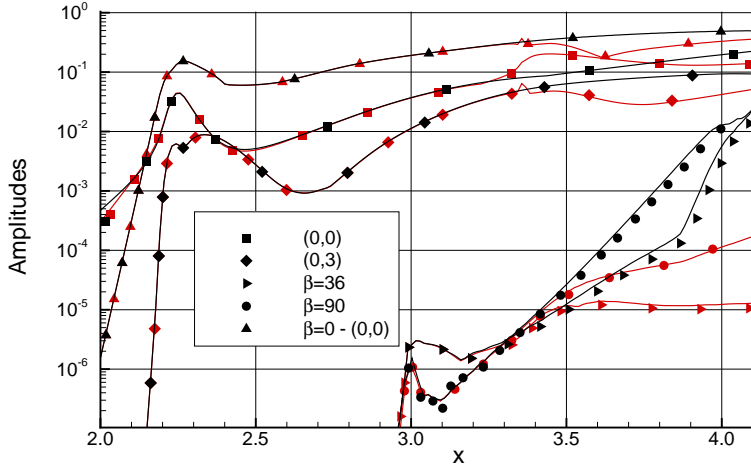


Figure 6. Downstream development of selected modal \bar{u}'_s -amplitudes from Fourier analysis in time (maximum over y or y & z , cf. Fig. 3). Shown are cases REF_i (black lines), REF_c (black symbols), 1-50p_i (red lines), and 1-50p_c (red symbols).

the lower end of the channel and the resulting mass flow $\dot{m} = \int (\rho v) r dr d\phi$ is sucked off the flow field. The diameter of the cylindrical channel is set up considering the theoretical mass flow of an assumed Hagen-Poiseuille profile and the mass flow from the modeled \cos^3 -distribution:

$$\dot{m}_{H-P} = |(\rho v)|_{max} \frac{\pi}{8} d_{H-P}^2 \quad (1)$$

$$\dot{m}_{mod} = |(\rho v)|_{max} \frac{2(3\pi - 7)}{9\pi} d_{mod}^2. \quad (2)$$

To obtain the same mass flows the diameter of the channel has to be decreased to $d_{chan}/d_{mod} \approx 0.66$, and considering our numerical grid we set $d_{chan} = 0.0168$. A channel length of $l_{chan} = 15d$ is chosen resulting in a nearly fully developed pipe flow at the lower outlet. For the current case our chosen pressure level yields an integrated $\dot{m}_{chan} = 4.718 \cdot 10^{-5}$ using the actual axial ρv -distribution in the channel, and we consequently prescribe $|(\rho v)|_{max,mod} = |-0.436|$ for the modeled case (with the \cos^3 -distribution) to obtain identical mass flows. The location of the suction hole center is adapted since the Ma=0.8 baseflow causes a slightly shifted vortex location, and $x = 3.3602$, $z = 0.0482$ has been used for the modeled case and the channel simulation.

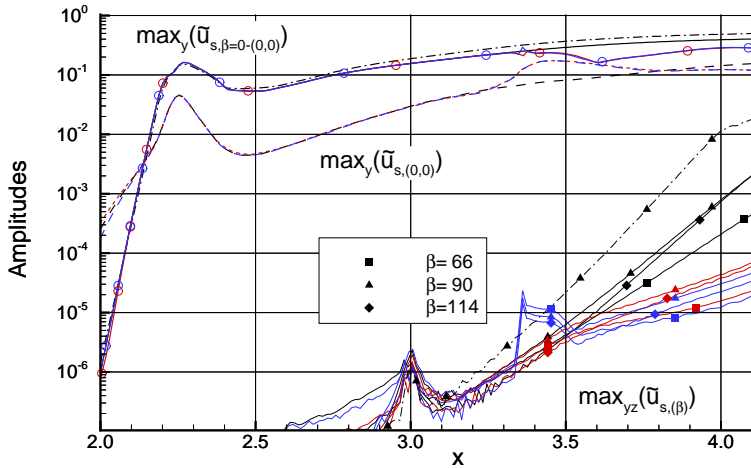


Figure 7. Downstream development of selected modal \bar{u}'_s -amplitudes from Fourier analysis in time (maximum over y or y & z , cf. Fig. 3). Shown are cases REF_{c,0.8} (black lines, without suction), 1-50p_{c,0.8} (red lines, with modeled suction), and 1-50p_{c,chan} (blue lines, comprising the suction channel flow). For comparison, the dash-dotted lines show $\beta = 0 - (0, 0)$ and $\beta = 90$ from the Ma=0.2 case.

The amplification of secondary modes for all three cases can be found in Fig. 7. All cases show slightly less amplitude growth for the CFV modes than in the $Ma=0.2$ case (dash-dotted line) which can be explained by less primary amplification as predicted by LST. This results also in lower secondary growth, probably due to the smaller amplitude level of the primary vortex. Transition to turbulence does not happen inside the considered integration domain for the reference case $REF_{c,0.8}$ (black lines). The influence of the modeled suction hole and the suction channel results in identical attenuation of the primary vortex, comparing the colored $\beta = 0 - (0, 0)$ - distributions. Moreover, this is true for the secondary-growth attenuation. The amplitude level of the three considered secondary modes is slightly higher for the modeled case at $x = 4.0$, but the growth rates match perfectly. Interestingly, for the case with channel, an amplitude peak of approximately 10^{-5} can be found at the location of the channel orifice ($x = 3.36$). These disturbances emerge from the channel which is confirmed by a Fourier analysis of the channel domain. However, these modes decay rapidly and soon after $x = 3.5$ the original secondarily unstable and now attenuated modes are traced again. The overall agreement for the modeled and channel case is excellent. We note that the channel Reynolds number based on the maximum suction velocity and d_{chan} is $Re = 675$, and well below the critical Reynolds number $Re_{crit} = 2300$ for pipe flow with sharp-edged inlet.

The flow fields of cases $1-50p_{c,0.8}$ and $1-50p_{c,chan}$ are compared in Fig. 8 and for visualization purposes we define a rotated coordinate system (ξ, y, ζ) where the y -axis is used as rotation axis and the angle $\phi = 49.25^\circ$ (clockwise positive in top down view) is chosen such that it coincides with the streamline-oriented coordinate system at the location of the hole center ($\xi = (x-x_0) \cos\phi + (z-z_0) \sin\phi$, $\zeta = -(z-z_0) \sin\phi + (z-z_0) \cos\phi$). If we select x_0 and z_0 to be the center of the suction hole and furthermore choose crosscuts at $\xi = 0.0$ and $\zeta = 0.0$ we obtain crosscuts of the flow fields in streamwise and spanwise direction. The agreement is again excellent. The streamlines coincide perfectly and also regions of positive ρv or negative u_r (velocity component in ξ -direction) are almost identical. The suction channel shows a large region of positive ρv (at the left side) indicating separation which could be a source of the disturbance generation observed in the Fourier plot. (Note that the line integrals of (ρv) over ξ at $\zeta = 0$ need not yield equal values for identical mass flow in both cases.) The maximum suction lies slightly downstream of the center of the channel. The lower channel outlet lies at $y = -0.25$, far from the domain shown. Note that, with included channel, the oncoming CFV could detrimentally influence the suction flow near the wall, but it does not.

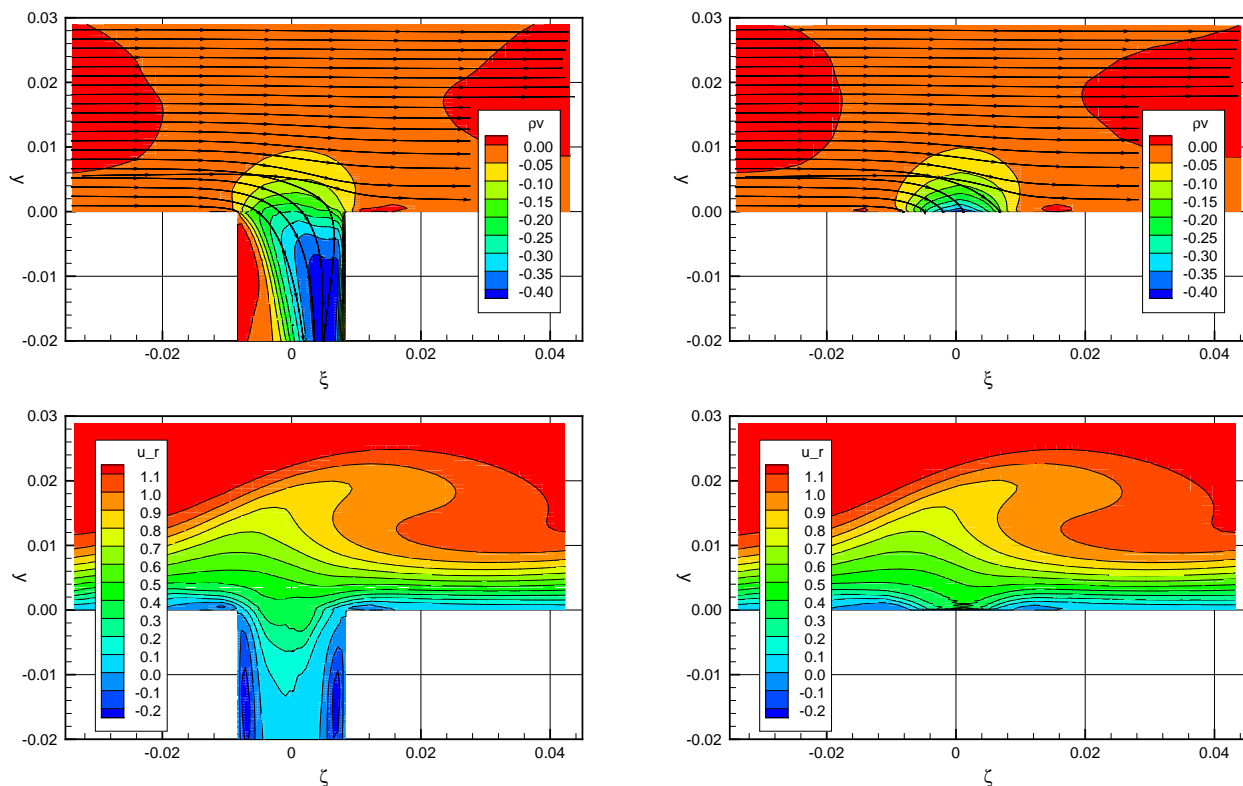


Figure 8. Crosscuts through the hole centers for cases $1-50p_{c,chan}$ (left) and $1-50p_{c,0.8}$ (right) in the rotated reference system ($x_0 = 3.360$ and $z_0 = 0.048$, hole center coordinates, $\phi = 49.25^\circ$, angle of the potential streamline at $x = 3.360$). Crosscuts at $\zeta = 0$ (top) show ρv -distributions and projected streamlines from the three-dimensional velocity flow field, crosscuts at $\xi = 0$ (bottom) show u_r -isocontours (velocity component in ξ -direction).

Fig. 9 shows a close-up of the vicinity of the suction channel inlet in the rotated reference system. The $y - \zeta$ crossplanes show u_r -velocity distributions (lines) and pressure distributions. The color levels are chosen to cover the spanwise variation of the vortex-induced pressure field in the first crosscut. The plane at $\zeta = 0.007$ shows the downstream pressure development. A distinct pressure minimum reveals the vortex core location in the first crosscut at $\zeta = 0.02$. When approaching the suction hole the pressure drops rapidly. Soon after the suction channel the pressure rises again quickly and the downstream influence of the strong suction is too severe to find a vortex-core related pressure minimum in the last crosscut. Six streamlines show the main-flow direction at $y = 0.027$. Close to the wall, five streamlines are shown that run into the suction channel and thus show the area of influence of the channel. A crosscut in the suction channel shows the ρv -distribution at $y = -0.046$.

The flow near the modeled wall-distribution of case 1-50 $p_{c,0.8}$ is compared to the the flow developing at the suction channel inlet for case 1-50 $p_{c,chan}$ in Fig. 10. The wall-pressure distribution is similar despite the three velocity components are fairly different. For the modeled case u_r and w_r are zero at the wall whereas in the case with suction channel values up to 0.3 are reached. However, the spanwise pressure variation induced by the vortices is far too small to be resolved by the selected scale. Also, no curling motion can be observed considering the anti-symmetric w_r -distribution as maybe expected in a scenario with oncoming vortices. The impact of the strong, localized suction on the flow field dominates CFV-induced deformation.

Vortical structures for all three considered cases are provided in Fig. 11 in a rotated reference system which covers approximately $3.0 < x < 4.2$. Subfigure a) shows the reference case. The CFVs grow in downstream direction and starting at $\xi = 1.0$ the small counter-rotating vortex can be found, see e.g. reference³. Subfigure b) shows the case with modeled suction, and c) provides the result from the simulation with included channel. The location of the suction holes are marked by black circles. The vortex is slightly pulled towards the wall. The secondary vortex disappears for both cases with suction suggesting a reduction of the strength of the primary CFV. Disregarding the very close region around the suction hole the results for the suction cases are identical.

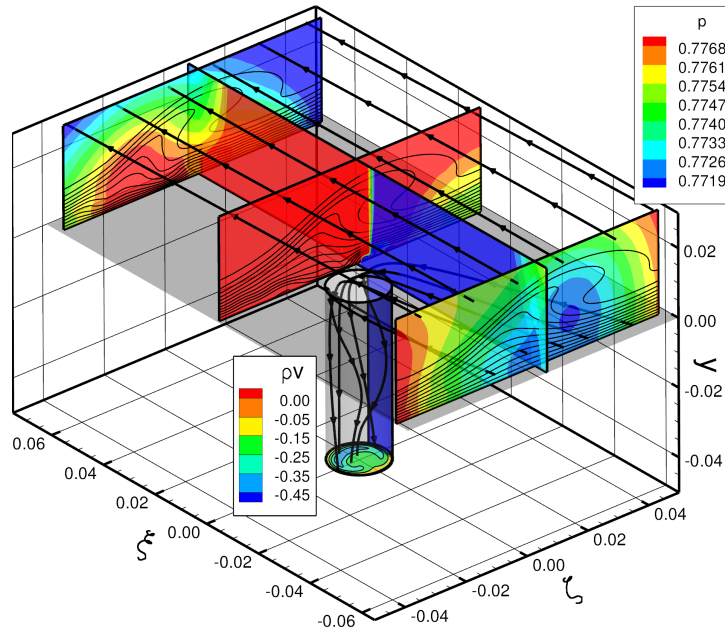


Figure 9. Details of the flow field at the suction channel inlet for case 1-50 $p_{c,chan}$. The rotated reference system is used (cf. Fig. 8 for details). Crosscuts show u_r -isocontours and ρv -isocontours inside the suction channel. Two groups of streamlines at different wall-normal distances are included (black lines).

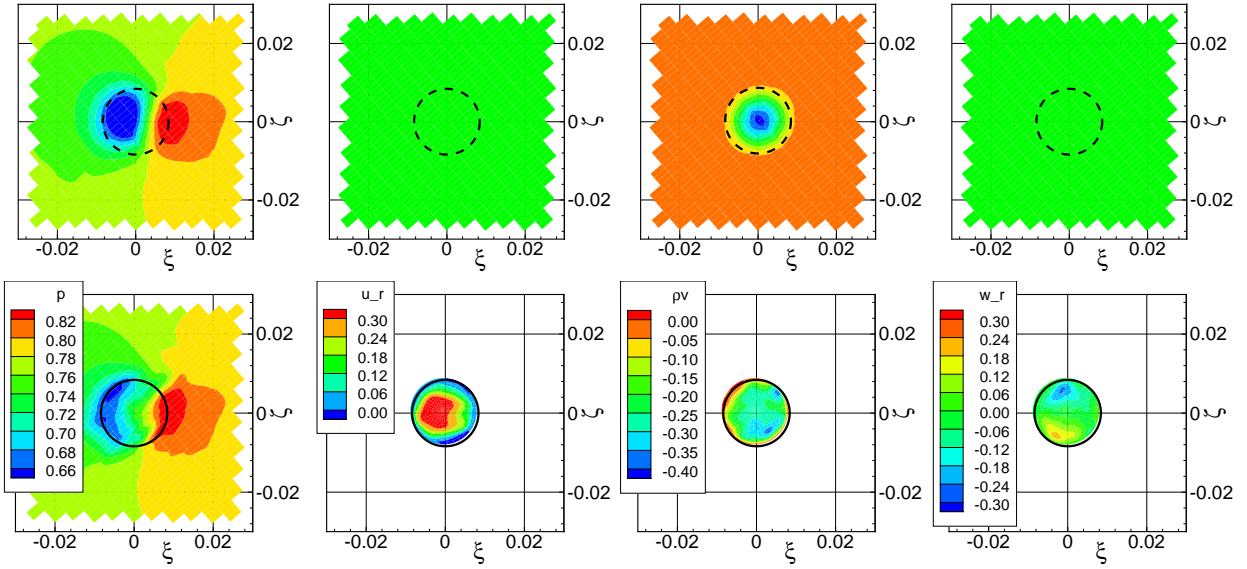


Figure 10. Top view on the suction hole for cases $1-50p_{c,0.8}$ (top) and $1-50p_{c,chan}$ (bottom). Shown are from left to right the wall-pressure p , the streamwise velocity component u_r , the wall-normal mass flux ρv , and the crossflow velocity w_r . Note that for case $1-50p_{c,chan}$ (bottom) the velocity crosscuts are located right beneath the surface. The black circles mark the channel diameter d_{chan} (dashed lines for comparison). The rotated reference system is used (cf. Fig. 8 for details). Color map inspired by Waikiki sunrise.

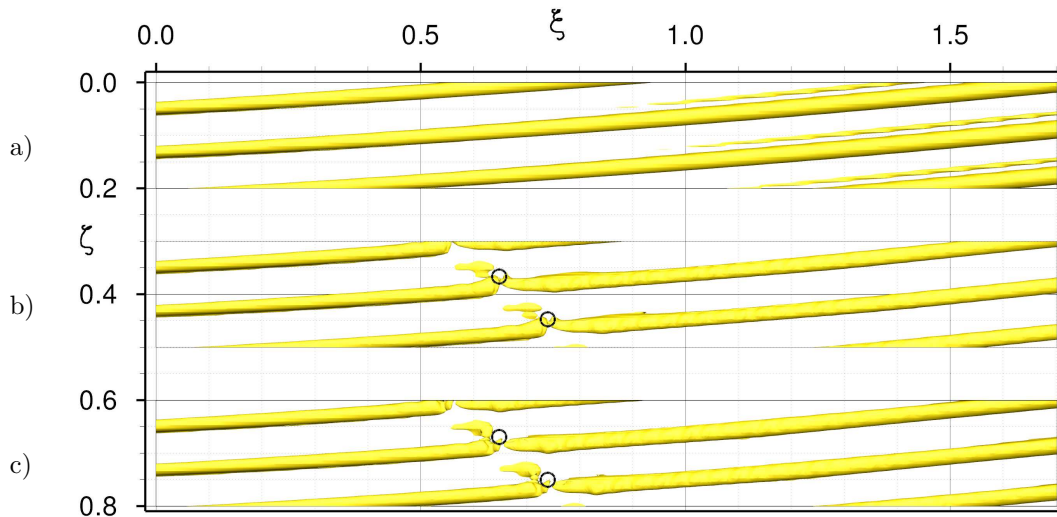


Figure 11. Top view of vortical structures (snapshot, $\lambda_2 = -5$) in rotated reference system with $x_0 = 3.0$, $z_0 = 0.0$, and $\phi = 49.25^\circ$. Shown are cases $REF_{c,0.8}$ (a), $1-50p_{c,0.8}$ (b), and $1-50p_{c,chan}$ (c). Ordinate ζ shifted by 0.25 and 0.5, respectively. Suction holes marked by black circles. Main flow is from left to right. 2.5 fundamental spanwise wave lengths are shown.

V. Conclusions

Transition control in three-dimensional boundary layers with crossflow has been investigated by means of spatial DNS. Strong, localized suction at the updraft side of an oncoming high-amplitude, steady crossflow vortex successfully delays transition to turbulence, attenuating or even neutralizing secondary instability. One selected pinpoint suction result from our incompressible numerical method employing one suction hole with $|v|_{max} = 0.5U_\infty$ is verified with our compressible method at $Ma=0.2$. So far, all suction holes have been modeled by the wall boundary condition, prescribing the wall-normal mass-flux distribution. At $Ma=0.8$, a case with one modeled suction hole has been compared to results achieved by a simulation that includes the full suction channel and hence the interaction with the oncoming flow. Fourier analysis in time and comparisons of the flow fields justify the application of modeled hole suction. The attenuation of the primary vortex and the growth of secondarily unstable modes is almost identical. This means that the interaction of the oncoming vortex with the suction flow near the wall is negligible in the considered case. The pressure variations caused by the vortex are much smaller than those caused by the strong suction itself. The same holds for the variations of the wall-normal velocity. Little doubt is left that the crucial value to be matched is the integral suction mass flow to obtain similar results.

Acknowledgments

The authors would like to thank O. Schmidt (IAG, University of Stuttgart) for providing the PNS code.

References

- ¹Babucke, A., Linn, J., Kloker, M.J., Rist, U.: Direct numerical simulation of shear flow phenomena on parallel vector computers. In High Performance Computing on Vector Systems 2005 (ed. M. Resch & al), Proc. High Performance Computing Center Stuttgart (HLRS), pp. 229-247, Springer (2006).
- ²Bippes, H.: Basic experiments on transition in three-dimensional boundary layers dominated by crossflow instability, *Progress in Aerospace Sciences*, vol. 35, pp. 363-412, 1999.
- ³Bonfigli, G., Kloker, M.J.: Secondary instability of crossflow vortices: validation of the stability theory by direct numerical simulation, *J. Fluid Mech.*, vol. 583, pp. 229-272, 2007.
- ⁴Friederich, T., Kloker, M.J.: Localized blowing and suction for direct control of the crossflow secondary instability, Seattle AIAA-2008-4394.
- ⁵Friederich, T., Kloker, M.J.: Numerical Simulation of Crossflow-Transition Control using Pinpoint Suction, in: New Results in Numerical and Experimental Fluid Mechanics VIII (eds. n.n.), NNFM, reviewed contributions to the 17. STAB/DGLR-Symposium, Nov. 2010, Berlin, Germany, 8 pages, in press, Springer
- ⁶Friederich, T., Kloker, M.J.: Direct Numerical Simulation of Swept-Wing Laminar Flow Control using Pinpoint Suction, in: High Performance Computing in Science and Engineering '10 (eds. W.E. Nagel, D.B. Kröner, M.M. Resch), Transactions of the HLRS 2010, pp. 231-250, Springer (2011).
- ⁷Kloker, M.J.: Advanced Laminar Flow Control on a Swept Wing Useful Crossflow Vortices and Suction, Seattle AIAA-2008-3835.
- ⁸Koch, W., Bertolotti, F. P., Stolte, A. and Hein, S.: Nonlinear equilibrium solutions in a three-dimensional boundary layer and their secondary instability, *J. Fluid Mech.*, vol. 406, pp. 131-174, 2000.
- ⁹Liepmann, H. W., Nosenchuck, D. M.: Active control of laminar-turbulent transition, *J. Fluid Mech.*, vol. 118, pp. 201-204, 1982.
- ¹⁰Linn, J., Kloker, M.J.: Numerical Investigations of Film Cooling. RESPACE - Key Technologies for Resuable Space Systems (ed. A. Gülhan), NNFM 98, pp. 151-169, Springer (2008).
- ¹¹Messing, R., Kloker, M.J.: Investigation of suction for laminar flow control of three-dimensional boundary layers, *J. Fluid Mech.* vol. 658, pp. 117-147, 2010.
- ¹²Peltzer, I., Wicke, K., Pätzold, A., Nitsche, W.: In-flight experiments on active TS-wave control on a 2D-laminar wing glove. *Seventh IUTAM Symposium on Laminar-Turbulent Transition*, Stockholm, Sweden, 2009 (ed. P. Schlatter & D. Henningson). Springer.
- ¹³Carpenter, A.L. Saric, W.S., and Reed, H.L.: Laminar Flow Control on A Swept Wing With Distributed Roughness, AIAA 2008-7335.
- ¹⁴Schrauf, G.: Status and perspective of laminar flow, The aeronautical journal (RAeAS), 109, no. 1102, 639-644.
- ¹⁵Wassermann, P., Kloker, M.: Direct numerical simulation of the development and control of boundary-layer crossflow vortices. In *New Results in Numerical and Experimental Fluid Dynamics II* (ed. W. G. Nitsche, H.-J. Heinemann & R. Hilbig). Proc. 11. AG STAB/DGLR Symposium (1998). Notes on Numerical Fluid Mechanics, vol. 72. Vieweg.
- ¹⁶Wassermann, P., Kloker, M.J.: Mechanisms and passive control of crossflow-vortex-induced transition in a three-dimensional boundary layer, *J. Fluid Mech.*, vol. 456, pp. 49-84, 2002.
- ¹⁷Wassermann, P., Kloker, M.J.: Transition mechanisms induced by travelling crossflow vortices in a three-dimensional boundary layer, *J. Fluid Mech.*, vol. 483, pp. 67-89, 2003.
- ¹⁸White, E. B., Saric, W. S.: Secondary instability of crossflow vortices, *J. Fluid Mech.*, vol. 525, pp. 275-308, 2005.